

Accelerating and guiding of electron beams in a cone target filled with near-critical-density plasmas

Jie-Jie Lan(蓝婕婕), Zhang-Hu Hu(胡章虎), and You-Nian Wang(王友年)

Citation: Chin. Phys. B, 2025, 34 (**12**): 125201. DOI: 10.1088/1674-1056/adea5b
http://cpb.iphy.ac.cn; http://iopscience.iop.org/cpb

What follows is a list of articles you may be interested in

Intense low-noise terahertz generation by relativistic laser irradiating near-critical-density plasma

Shijie Zhang(张世杰), Weimin Zhou(周维民), Yan Yin(银燕), Debin Zou(邹德滨), Na Zhao(赵娜), Duan Xie(谢端), and Hongbin Zhuo(卓红斌)
Chin. Phys. B, 2023, 32 (**3**): 035201. DOI: 10.1088/1674-1056/ac872c

Correction of intense laser-plasma interactions by QED vacuum polarization in collision of laser beams

Wen-Bo Chen(陈文博) and Zhi-Gang Bu(步志刚)
Chin. Phys. B, 2023, 32 (**2**): 025204. DOI: 10.1088/1674-1056/ac70b3

The inverse Bremsstrahlung absorption in the presence of Maxwellian and non-Maxwellian electrons

Mehdi Sharifian, Fatemeh Ghoveisi, Leila Gholamzadeh, Narges Firouzi Farrashbandi
Chin. Phys. B, 2019, 28 (**10**): 105202. DOI: 10.1088/1674-1056/ab4173

Properties of long light filaments in natural environment

Shi-You Chen(陈式有), Hao Teng(滕浩), Xin Lu(鲁欣), Zong-Wei Shen(沈忠伟), Shuang Qin(秦爽), Wen-Shou Wei(魏文寿), Rong-Yi Chen(陈荣毅), Li-Ming Chen(陈黎明), Yu-Tong Li(李玉同), Zhi-Yi Wei(魏志义)
Chin. Phys. B, 2018, 27 (**8**): 085203. DOI: 10.1088/1674-1056/27/8/085203

Laser-driven relativistic electron dynamics in a cylindrical plasma channel

Pan-Fei Geng(耿盼飞), Wen-Juan Lv(吕文娟), Xiao-Liang Li(李晓亮), Rong-An Tang(唐荣安), Ju-Kui Xue(薛具奎)
Chin. Phys. B, 2018, 27 (**3**): 035201. DOI: 10.1088/1674-1056/27/3/035201

Accelerating and guiding of electron beams in a cone target filled with near-critical-density plasmas

Jie-Jie Lan(蓝婕婕), Zhang-Hu Hu(胡章虎)†, and You-Nian Wang(王友年)

School of Physics, Dalian University of Technology, Dalian 116024, *China*

(Received 29 April 2025; revised manuscript received 19 June 2025; accepted manuscript online 1 July 2025)

Direct laser acceleration is one of the mechanisms for producing electron bunches carrying up to μC charge, which has attracted much attention in recent decades. Currently, one major challenge for its applications to high-flux x-ray beams and Compton γ-ray sources is the relatively large divergence angle (hundreds of mrad). In this work, a scheme to guide and focus the incident laser and the accelerated electrons is proposed and tested through two-dimensional (2D) particle-in-cell (PIC) simulations. The scheme is based on a hollow cone target (made of aluminum or gold) filled with near-critical-density (NCD) plasmas (pre-ionized polymer foams). Instead of separating the acceleration and focusing processes, it is convenient to simultaneously realize both requirements in such an NCD plasma-filled cone target. PIC simulations reveal that the laser, electrons, and emitted photons can be well-guided along the cone axis in the NCD plasma-filled cone target, preserving the characteristic of high beam charge. Detailed PIC simulations are also performed to show the dependence of the electron energy and charge on the plasma density for a given laser.

Keywords: laser–plasma interactions, direct laser acceleration, plasma-filled cone target, electron beams

PACS: 52.38.–r, 52.38.Kd, 52.38.Hb, 52.40.Fd

DOI: 10.1088/1674-1056/adea5b **CSTR:** 32038.14.CPB.adea5b

1. Introduction

Electron beams with high quality are nowadays widely used for many applications such as, for instance, bright γ-ray sources,[1,2] free electron lasers (FELs),[3–5] and the generation of electron–positron pairs.[6–8] The applications (e.g., FELs) that prioritize a narrow energy spectrum tend to rely on the conventional RF[9] or laser-wakefield[10–12] accelerators. Whereas the applications (e.g., high brightness x/γ-rays and the creation of electron–positron pairs) that prioritize a high beam charge tend to rely on the direct laser acceleration (DLA).[13–16] It has been demonstrated that the DLA can generate high-energy electron beams with a charge[17,18] of hundreds nC or even μC using upcoming multi-petaWatt laser facilities. Such a bunch carrying large charges has become an important research topic in recent decades because it represents a useful source of high-energy electrons itself and its significance in enhancing the brightness of the radiation, material detection,[19] and radiotherapy treatment.

In the DLA process of ultraintense laser pulses interacting with the NCD plasmas, the accelerated electron beams gain energy directly from the incident laser,[20,21] and the experimental evidence of the DLA-accelerated electrons has been observed.[22,23] However, when the laser pulse propagates into plasmas for a relatively long distance, it will undergo transverse tilt due to the filamentation and hosing instabilities.[23–26] This will result in the generation of uncontrollable off-axis electrons with relatively large divergence angles and hinder their further applications.[27,28] Up to now, there have been numerous efforts to suppress the instability and simultaneously increase the energy conversion efficiency from laser to relativistic electrons.

One way is to control the laser beam itself. It has been proposed that the filamentation instability can be mitigated for the laser beam with an elliptically distributed profile.[29,30] In addition, the DLA electron energy dependency on laser focusing geometry has been investigated using experiments and numerical modeling.[21] Using a hollow solid plasma conical target, 2D PIC simulations[31] have predicted a laser intensity enhancement by a factor of 10. The scaling between the laser intensity and the electron energy cutoff has been analytically given in Ref. [15]. On the other hand, structured plasma targets open a way to generate dense forward-moving electrons in a given laser condition. Theoretical analyses and simulations performed by Huang *et al.* have shown that the laser hosing instability can be mitigated and even suppressed by using a relatively steep parabolic plasma channel.[24] The instability can also be suppressed in a target consisting of a material-filled cylindrical channel.[32] In this case, the incident laser field can efficiently accelerate electrons propagating along the forward direction in the quasistatic azimuthal magnetic fields, which can confine electrons in the transverse direction. Moreover, with the advancement of the three-dimensional (3D) nanofabrication technique, micro-cylinder and -tube targets have been designed and used in experiments to manipulate either the particles or laser pulses.[33,34] In addition, electron accel-

†Corresponding author. E-mail: zhanghu@dlut.edu.cn

© 2025 Chinese Physical Society and IOP Publishing Ltd. All rights, including for text and data mining, AI training, and similar technologies, are reserved.

eration and x-ray generation from NCD nanotube foams driven by moderately relativistic lasers have been reported.[35,36]

Recently, structured targets with an initially empty cone have been proposed to reduce the energy requirement in the inertial confinement fusion scheme,[37–40] and improve high-intensity laser–matter interaction[41] and the focusing ability of the incident laser pulses.[27,31] Using an opening gold cone filled with hydrogen plasma can generate high-energy-density electron jet[42] and highly-polarized high-energy brilliant γ-rays.[43] Energetic and collimated proton beams have also been observed inside a conical target with 2D PIC simulations.[44] It has been demonstrated that low-density polymer foams pre-ionized by a well-controlled ns pulse are excellent plasma targets to trigger DLA of electrons by sub-picosecond relativistic laser pulses.[14,45–47] Furthermore, the use of foam materials in experiments imposes less stringent constraints on laser contrast and pointing stability, making them attractive targets for laser–plasma interaction studies. With these advancements, we propose a method to guide and focus the incident laser and DLA-accelerated electrons based on a foam-filled cone target, as shown schematically in Fig. 1(b). Simulations reveal that the laser pulse and thus the DLA-accelerated electrons are off-axis in the case of NCD plasma target [see Fig. 1(a)]. While employing a cone target, the incident laser, accelerated electrons, and the emitted photons can be well-guided along the cone axis because of the strong azimuthal magnetic fields[48] generated by the beam current. The magnetic field increases linearly to the maximum at the inner walls of the cone and then decreases rapidly within the thin layer of plasma skin depth. In addition, the characteristic of high beam charge can be reserved. This paper is organized as follows. The PIC simulation setup is presented in Section 2. In Section 3, we discuss the generation of strong azimuthal magnetic fields and the effective guiding in the NCD plasma-filled cone target and thus the suppression of the hosing instability. The corresponding radiated photon properties are also compared. In Section 4 the influences of the NCD plasma density and the case of laser injected off-axis are discussed. And finally, we summarize the work in Section 5.

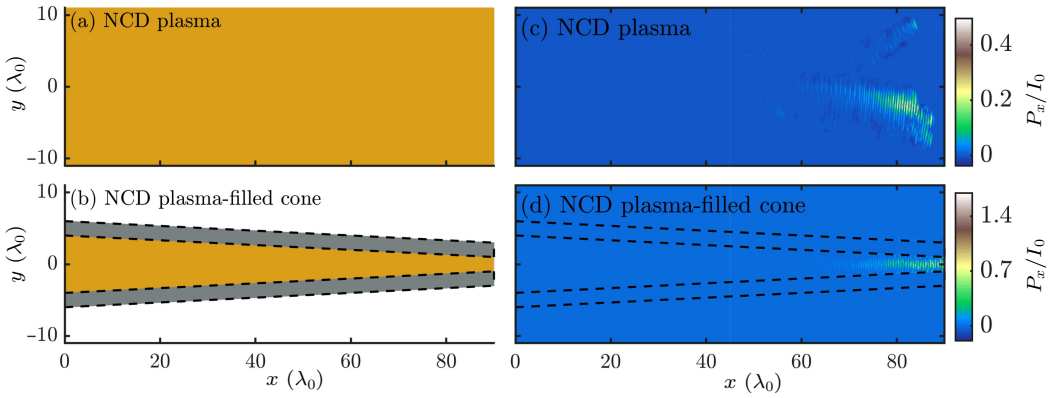


Fig. 1. The initial density profiles of NCD plasma (a) and NCD plasma-filled cone (b) targets. The density of the NCD plasma and the cone are set as $n_{e1} = 1.79\,n_c$ and $n_{e2} = 89.69\,n_c$, respectively. The longitudinal Poynting fluxes (normalized to initial laser intensity I_0) at $t = 480$ fs in these two cases are shown in panels (c) and (d). In addition, the dashed black lines mark the boundary of the cone in panels (b) and (d) for illustration, and $\lambda_0 = 1$ μm is the wavelength of the laser pulse.

2. PIC simulation setup

To model the laser–plasma interaction in the DLA regime, 2D PIC simulations have been performed using the code EPOCH.[49] A linearly polarized (in y-direction) laser pulse with an intensity of $I_0 = 5 \times 10^{21}$ W/cm^2 (corresponding to $a_0 = |e|E_0/m_e c\omega_0 \approx 60$) and the central wavelength of $\lambda_0 = 1$ μm is irradiated from the left boundary of the simulation box. Here, E_0 is the electric field amplitude of the laser, c is the speed of light in vacuum, and m_e (e) is the electron mass (charge). The laser pulse has Gaussian spatial and temporal profiles as $a = a_0\,\mathrm{e}^{(-y^2/\sigma^2 - t^2/\tau^2)}$ with $\sigma = 1.3\lambda_0$ and $\tau = 80$ fs. The central axis of the incident laser pulse is aligned with $y = 0$. The simulation box is featured as $120\lambda_0 \times 22\lambda_0$ in $x \times y$ directions, and the cell size is set to be $\Delta x = \Delta y = \lambda_0/40$. Moreover, the absorbing boundary conditions are employed for both the laser field and particles. We represent electrons and ions by 16 and 10 macroparticles per cell. Two different targets (NCD plasma and NCD plasma-filled cone targets) with the length of $90\lambda_0$ are examined, as illustrated in Fig. 1. The NCD plasma electron density is set to be $n_{e1} = 2 \times 10^{27}$ m^{-3} $\approx 1.79\,n_c$ with a mean ion charge state of 3 as shown in Ref. [46], where n_c is the critical density. Additionally, the density of the cone is set as $n_{e2} = 1 \times 10^{29}$ m^{-3} $\approx 89.69\,n_c$ with a thickness of $2\lambda_0$ [see the dashed black lines in Fig. 1(b)]. In experiments, gold or aluminum is often used as the cone material, and the incident laser can be reflected upon hitting the cone wall. The left and right opening radii of the cone are $4\lambda_0$ and λ_0, respectively. It should be noted that the laser intensity I_0 used in this work is much larger than that required for ionizing gold ($\sim 1 \times 10^{17}$ W/cm^2). Therefore, the edge of the laser pulse is enough to ionize the cone target to form plasmas.

3. Electron acceleration and guiding

Laser pulses with hundreds of fs duration propagating through NCD plasmas are favorable for the electron acceleration in DLA regime. In this process, the DLA-accelerated electrons gain energy directly from the laser. The ponderomotive force expels electrons thus creating an ion channel. The transverse laser electric field E_y attracts electrons toward the center axis of the laser pulse. This can be clearly seen from Fig. 2(a), in which the red dash-dot rectangular region represents the attracted DLA-accelerated electrons: the microbunched electron beam with period $\sim \lambda_0$ is a typical characteristic of the DLA regime. After being injected into the ion channel, the electrons oscillate in the transverse electric field of the laser and then the $\boldsymbol{v} \times \boldsymbol{B}$ force deflects the transverse velocity into the longitudinal direction, and finally the accelerated electrons co-move forward with the laser pulse. When the laser pulse propagates into the plasma for a relatively long distance, the laser hosing instability would grow inevitably (see Fig. 1(c)). The instability can lead to the generation of off-axis electrons, as can be clearly seen from Figs. 2(b) and 2(c). To better illustrate the off-axis electrons induced by the hosing process of the laser pulse, the energy-angular distribution for DLA-accelerated electrons at $t = 480$ fs is shown in Fig. 3(a), where the angle is defined as atan(y/x). In this case, the electron angular distribution spans from $-8°$ to $8°$. While employing an NCD plasma-filled cone target [see Fig. 1(b)], the incident laser (shown in Fig. 1(d)) and thus accelerated electrons can be well-guided along the cone axis, as illustrated in Fig. 3(b) by the black solid arrow. And the electrons only occupy a smaller angular range (between $-0.5°$ and $0.5°$). It must be pointed out that the hosing instability can be suppressed [see Figs. 1(d) and 2(f)] and the collimation of the electron beam can be improved using the NCD plasma-filled cone target. Additionally, comparisons between the lines in Fig. 3(c) show that the charge of the accelerated beam can be reserved. This indicates a high acceleration efficiency with a cone target.

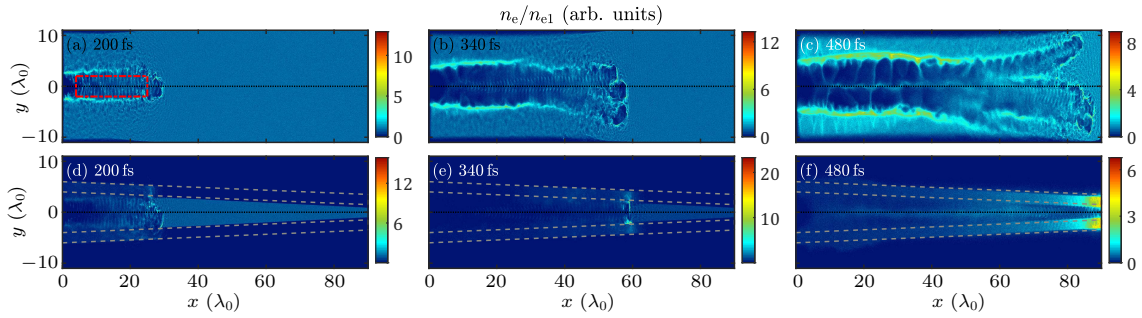


Fig. 2. Distributions of the electron density n_e (normalized to the initial NCD plasma density n_{e1}) at the cases of NCD plasma [(a)–(c)] and NCD plasma-filled cone [(d)–(f)] targets at $t = 200$ fs [(a), (d)], 340 fs [(b), (e)], and 480 fs [(c), (f)]. The red dash-dot rectangular region in panel (a) represents the DLA-accelerated electrons attracted to the center axis of the laser pulse. In addition, the black dotted lines illustrate the center axis of the initial incident laser pulse at $y = 0$.

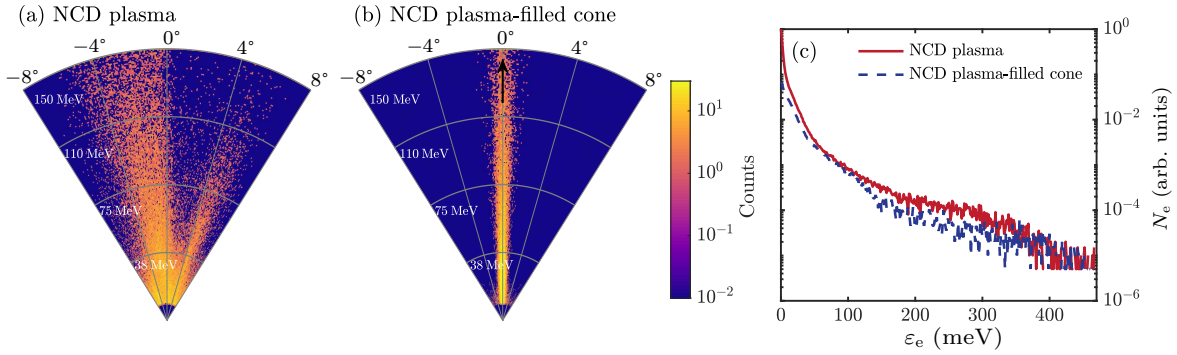


Fig. 3. Energy–angular distributions for the cases of NCD plasma (a) and NCD plasma-filled cone (b) targets at $t = 480$ fs with energies between 10 MeV–150 MeV. The black solid arrow indicates the direction of the incident laser pulse, i.e., $y = 0$. Additionally, the colorbar presents the counts of electrons. The corresponding electron energy spectra for the two targets are also shown in panel (c). It should be noted that the angle is defined as atan(y/x).

The suppression of the hosing instability in an NCD plasma-filled cone target can be understood as follows. Firstly, the laser ponderomotive force pushes away the electrons from the laser axis, leading to a local decrease in the plasma frequency and an increase in the refractive index, $n = \sqrt{1 - n_e/\gamma_0 n_c}$. Here, $\gamma_0 = \sqrt{1 + a_0^2/2}$ is the Lorentz factor. As a result, the laser pulse and thus the electrons tend to bend towards the area of larger refractive indexes, i.e., the laser axis, which can be seen from both targets in Fig. 2. More importantly, as the laser pulse travels through the NCD plasma-filled cone target, a plasma return current can be induced with the average velocity v_e moving backward along the

cone inner surface. This return current localizes at the edge of the laser, and thus the current of the accelerated beam remains unneutralized.[32] Furthermore, the ion response time $1/\omega_{\rm i} \approx 60$ fs is shorter than that of the laser duration. Thus the ions have sufficient time to keep charge neutralization and reduce the electric field, which has also been clearly discussed in Ref. [32]. Therefore, the electric field E_y and magnetic field B_z are no longer canceled. Strong transverse electromagnetic fields ($E_y - cB_z$ dominated by the quasi-static self-generated fields in the plasmas) up to 10^{14} V/m can be generated in the inner walls, and the DLA-accelerated electrons can be focused by the self-generated magnetic fields. As shown in Fig. 4, the maximum field strength in the cone inner surface (as marked by the solid black ellipses in panel (b)) is about 1.5×10^{14} V/m at $t = 480$ fs, which is boosted by a factor ~ 6 compared to the case of NCD plasma target in panel (a). When the laser and thus the DLA-accelerated electrons arrive at the cone tip, the radius of the electron bunch is about $R = \lambda_0$, i.e., the right opening radius of the cone. From Ampere's law, the transverse magnetic field in the NCD plasma-filled cone target can be expressed as

$$\begin{aligned} B_z &= \frac{\mu_0 I_{\rm b}}{2\pi R^2} r \qquad (r < R), \\ &= \frac{\mu_0 I_{\rm b}}{2\pi r} \qquad (R < r \lesssim (R + c/\omega_{\rm pe})), \end{aligned} \tag{1}$$

where μ_0 is the permeability of vacuum, $I_{\rm b}$ is the DLA accelerated electron current, and $\omega_{\rm p} = \sqrt{n_{\rm e1} e^2/\varepsilon_0 m_{\rm e}}$ is the NCD plasma electron frequency with ε_0 being the vacuum permittivity. From Eq. (1), the magnetic field increases linearly to the maximum at the inner walls and then decreases rapidly within the thin layer of plasma skin depth $c/\omega_{\rm p}$, as indicated in Fig. 4(b). With the assumptions that the electron beam, propagating along the x-direction with velocity $\sim c$, is cylindrically symmetric and has a uniform density $n_{\rm b} = n_{\rm e}^{\rm max}/2 \approx 3n_{\rm e1}$ as shown in Fig. 2(f), the beam current can be deduced as $I_{\rm b} = n_{\rm b} ec\pi R^2 = 0.9$ MA. Thus the maximum magnetic field within the cone's inner surface is about $B_z^{\rm max} = \frac{\mu_0 I_{\rm b}}{2\pi R} \approx 1.8\times10^5$ T, which shows agreement with the simulation results ($c\langle B_z\rangle = 2.2\times10^{13}$ V/m as shown in Fig. 4(c), which is larger than that of the quasi-static self-generated electric field $\langle E_y\rangle$). With such extremely strong magnetic fields, the accelerated electrons can be well guided along the cone axis and the hosing instability can be suppressed [see Figs. 1(d) and 2(f)]. It is assumed that the DLA electron beams in both targets carry identical currents. In the case of NCD plasma, however, the radius of the plasma cavity is approximately $5\lambda_0$ (see Figs. 2(b) and 2(c)), which is five times larger than that the case considering a cone. According to Eq. (1), the self-generated magnetic field B_z in the NCD plasma-filled cone target is consequently enhanced by a factor of five. This can also be obtained from comparing Figs. 4(a) and 4(b). Moreover, as the laser pulse moves forward and the cone radius decreases, the strength of the magnetic field $B_z^{\rm max} \sim 1/R$ can increase further, showing good agreement with Fig. 4(b). However, the right opening radius of the cone cannot be reduced indefinitely because of the diffraction-limited value.[31]

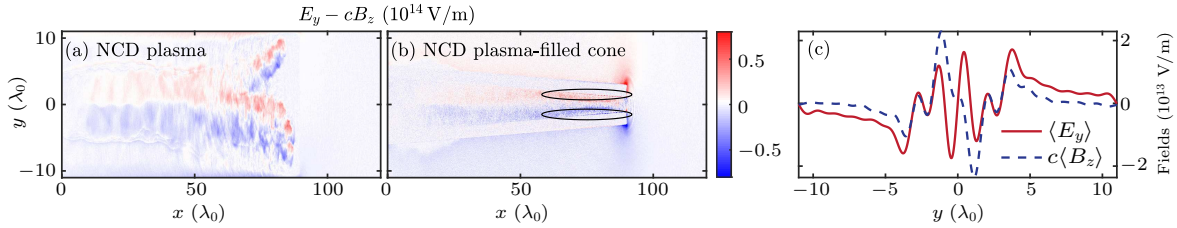


Fig. 4. Distributions of the transverse electromagnetic field ($E_y - cB_z$) for the cases of NCD plasma (a) and NCD plasma-filled cone (b) targets at $t = 480$ fs. The solid black ellipses in panel (b) mark the strong field in the inner walls. The corresponding slice profiles of the quasi-static self-generated electric field $\langle E_y\rangle$ and magnetic field $c\langle B_z\rangle$ in the cone target at $x = 78$ μm are also displayed in panel (c).

Figure 5 shows the trajectories of two selected electrons in the targets. As the tracked electrons travel through the target, they lose and gain energies at specific locations. In this figure, one can clearly observe that the electron in the NCD plasma target experiences serious transverse tilting, i.e., hosing instability, for a relatively long propagation distance (about 50 μm). In contrast, the laser in the NCD plasma-filled cone target can be well-guided along the center axis (see Fig. 1(d)), and so will the accelerated electron. The advantage of such an NCD plasma-filled cone target is obvious that the tilting behavior can be suppressed because of the transverse focusing field (dominated by the self-generated magnetic field $\langle B_z\rangle$ shown in Fig. 5) discussed before. It should be noted that the instability is a 3D process, 2D PIC simulations may overestimate its growth rate.[50] However, limited by the present computation capabilities, the current work is restricted to two dimensions. Nevertheless, the cone structure retains its advantages in guiding both the laser pulse and the accelerated electron beam. The oscillations of the electrons can also be observed in this figure, suggesting the DLA mechanism. The electron energy is shown to increase over multiple oscillations in the laser pulse.

It should be noted that the trapped electrons behind the laser wave front and confined near the laser axis oscillate significantly in the transverse direction (which can be clearly seen from Fig. 5) and emit synchrotron-like gamma photons in both

forward and backward directions. We further show here the effect of the cone target on the properties of emitted photons. The energy–angular distributions of the photons in the two targets at $t = 480$ fs are shown in Figs. 6(a) and 6(b). Only the photons with energies between 1 MeV–10 MeV and velocities $v_x > 0$ are counted in the figure. It must be pointed out that the DLA-accelerated electrons in the case of NCD plasma target are uncontrollable and their deflecting angle would exhibit random behavior in every simulation. As shown in Fig. 6(a), the emission photons are located from $-20°$ to $10°$, showing a great emission angle. After changing the NCD plasma target to an NCD plasma-filled cone target, the transverse oscillation of the trapped electrons can be confined by the electromagnetic fields in the cone. Thus the angle of emission can be greatly decreased, and the photons are also well-guided along the cone axis, as clearly shown in Fig. 6(b). In addition, the transverse electromagnetic fields would result in a larger cut-off energy of the photons in the cone target. Figure 6(c) shows the corresponding photon energy spectra in the two targets. In this figure, the number of photons increases, and the cut-off energy increases by a factor of two using an NCD plasma-filled cone target proposed in this work (not shown here). These results are of great interest for applications in high-energy-density experiments, which require a high photon flux. It is also noteworthy that both the cutoff energy and flux of the photons propagating in the backward direction (i.e., $p_x < 0$) increase significantly in the NCD plasma-filled cone target, as illustrated in Fig. 6(d). These photons are primarily generated through nonlinear Compton scattering, where relativistic electrons interact with the intense laser field and emit high-energy photons in the opposite direction of the laser propagation. The emission of backward x-rays has been experimentally reported.[51] Such backward-propagating gamma photons may be highly beneficial for applications such as nuclear spectroscopy, high-resolution imaging, and the development of compact photon sources.

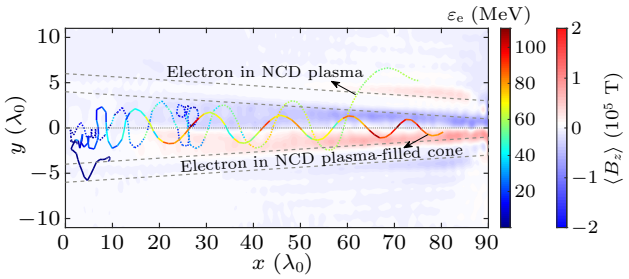


Fig. 5. Trajectories of the DLA-accelerated electron in the cases of NCD plasma and NCD plasma-filled cone targets. The dotted line is used to illustrate the center axis of the initial incident laser pulse. The colorbar presents the energy of electrons. In addition, the self-generated magnetic $\langle B_z \rangle$ and the boundary illustrating the cone target have been added for illustration.

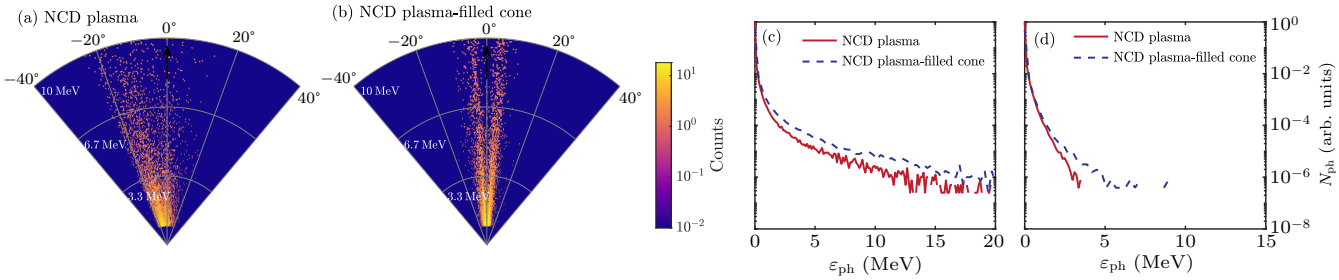


Fig. 6. The energy–angular distributions of the DLA-associated synchrotron-like radiation photons for the cases of NCD plasma (a) and NCD plasma-filled cone (b) targets at $t = 480$ fs with energies between 1 MeV–10 MeV. The black solid arrows indicate the direction of the incident laser pulse, i.e., $y = 0$. The colorbar presents the counts of photons. The corresponding photon energy spectra for the two targets is shown in panel (c). In addition, panel (d) shows the spectra of photons propagating in the backward direction, i.e., $p_x < 0$.

4. Effects of target parameters

Next, simulations are also performed to find out the dependence of the electron energy, charge, and divergence angle on the plasma density for a given laser. By changing the delay time between the ns and ps laser pulses in experiments, the ps laser can interact with the NCD plasma with different densities. The density plays an important role in increasing electron energy and laser absorption efficiency during the DLA acceleration stage. Here, three different densities are considered: $0.36\,n_c$, $1.79\,n_c$, and $5.38\,n_c$ with other parameters unchanged. A summary of the results at $t = 480$ fs is shown in Fig. 7: the electron energy spectra (a), and the angular distributions of photons with energies between 1 MeV–10 MeV (b) for different densities. Here, $\theta = \mathrm{atan}(p_y/p_x)$ is the divergence angle of photons. From this figure, we can infer that there exists an optimal NCD plasma density in our laser–plasma parameters, i.e., $n_e = 1.79\,n_c$. It is found from Fig. 7(a) that the charge of high-energy (20 MeV–120 MeV) electrons in the case of $n_e = 1.79\,n_c$ is enlarged by a factor of 1.3 compared with $n_e = 5.38\,n_c$, and a factor of 6.8 compared with $n_e = 0.36\,n_c$. In the case of low density, i.e., $n_e = 0.36\,n_c$, the laser can transport in the cone without significantly weakening, leading to a limited number of the DLA accelerated electrons and radiated photons, as can be seen from the red dashed lines in Fig. 7. For a higher density plasma with $n_e = 5.38\,n_c$, more electrons can be trapped in the initial interaction stage between laser and plasmas. Therefore, the laser is rapidly exhausted in the cone, and background electrons are piled up in the laser front so that

the laser cannot penetrate deeper into the plasma.[52] In this case, the trapped electrons are only accelerated to low energy, and the photons are emitted with a relatively broad angular distribution. When the NCD plasma density is $1.79n_c$, the angular distribution of photons [see Fig. 7(b)] becomes narrow, indicating that most photons are emitted in the forward direction.

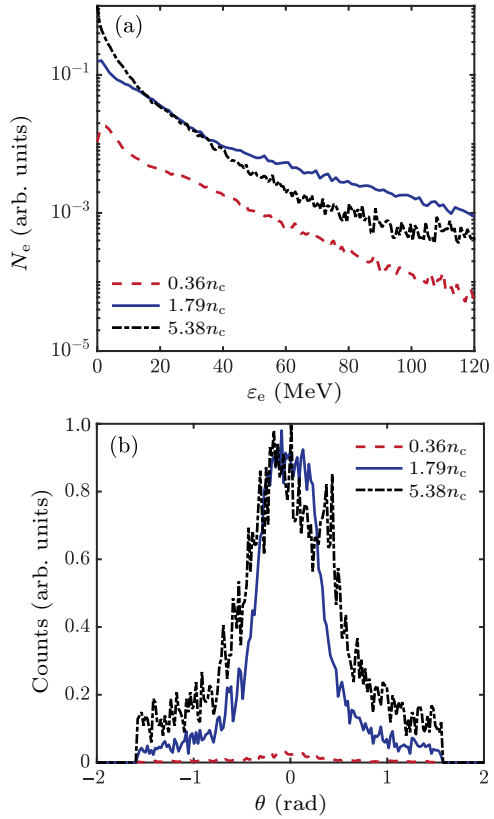


Fig. 7. The energy spectra of accelerated electrons (a), and the divergence angle atan(p_y/p_x) of photons with energies between 1 MeV–10 MeV (b) for different densities at $t = 480$ fs.

Furthermore, the case of laser injected off-axis is considered, which is a scenario commonly encountered in experiments. In this case, the parameters of the target are similar to those presented in Section 2. Simulations reveal that as the laser injection becomes increasingly off-axis (quantified by the transverse displacement Δy from the laser axis to the x-axis), the beam charge decreases while its divergence angle increases. As shown in Fig. 8(a), when the off-axis distance is $1.5\lambda_0$, the beam charge decreases by 30%, and the divergence angle increases by 20%. Additionally, with the same cone length and left opening radius, evolutions of the dimensionless FWHM (full width at half maximum) divergence angle for different right opening radii $r_{\rm out}$ have been considered, i.e., different cone angles. As illustrated in Fig. 8(b), the divergence angle remains relatively stable as the radius varies, especially in the case of $I_0 = 1\times10^{20}$ W/cm^2. These results demonstrate the robustness of the NCD plasma-filled cone target. The effects of the laser obliquely incident at a small angle on the electron beam charge and divergence angle have also been considered. To simplify the simulation, the laser is set to propagate along the x-axis, while the cone target is placed with a certain inclination angle $\alpha = 0.57°$, 2.86°, and 5.71°. Here, α is defined as the angle between the cone axis and the x-axis as shown in Fig. 9(c). Before the laser hits the cone walls, the longitudinal poynting fluxes remain consistent in these cases (as illustrated in

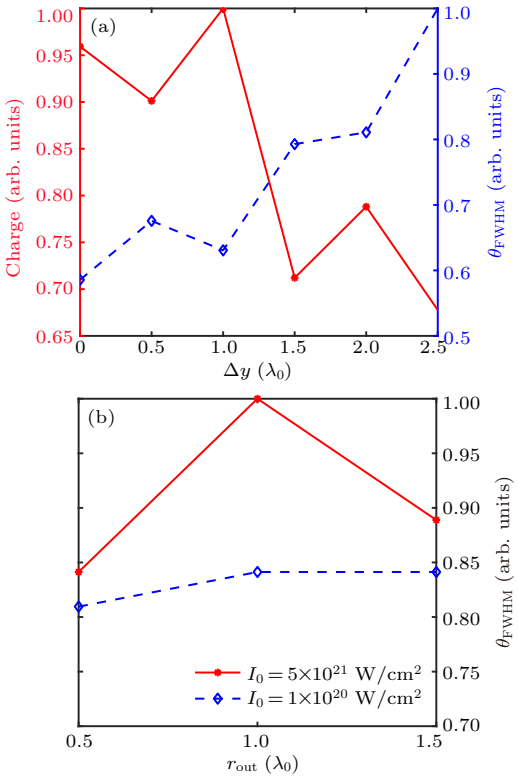


Fig. 8. (a) Evolutions of the beam charge and the dimensionless FWHM divergence angle for different off-axis Δy. Here, Δy is defined as the distance from the laser incident axis to the x-axis. (b) Evolutions of the dimensionless FWHM divergence angle for different right opening radii $r_{\rm out}$, i.e., different cone angles.

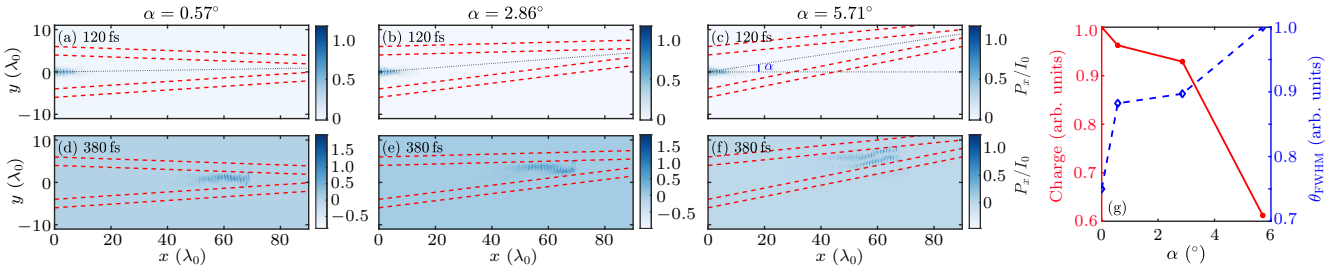


Fig. 9. Distributions of the longitudinal Poynting fluxes (normalized to initial laser intensity I_0) at the cases of $\alpha = 0.57°$ [(a), (d)], 2.86° [(b), (e)], and 5.71° [(c), (f)] at $t = 120$ fs [(a)–(c)] and 380 fs [(a)–(c)]. The corresponding evolutions of the beam charge and the dimensionless FWHM divergence angle for different inclination angles α. Here, α is defined as the angle between the cone axis and the x-axis as shown in panel (c).

Figs. 9(a)–9(c)). Although there exists an inclination angle between the laser axis and the cone axis, the laser is eventually guided to propagate along the direction of the cone axis, which can be seen from Figs. 9(d)–9(f). The corresponding evolutions of the beam charge and the dimensionless FWHM divergence angle for different inclination angles α are shown in Fig. 9(g). From this figure, to maintain a high beam charge and a small divergence angle, α should be less than 2.86°.

5. Conclusion

In conclusion, a novel target in DLA has been proposed and validated by 2D PIC simulations. The scheme is based on a hollow cone filled with NCD plasmas, which can be conveniently obtained in experiments. PIC simulations reveal that the laser pulse and thus the DLA-accelerated electrons are off-axis in the case without a cone. When using an NCD plasma-filled cone target, the maximum transverse field strength increases by a factor of six. In this case, the laser, DLA-accelerated electron beam, and the emitted photons can be well guided along the cone axis. Additionally, the characteristic of high beam charge can be preserved. Based on this scheme, the electron acceleration and focusing processes can be achieved simultaneously, highlighting the key advantage of our approach. The cut-off energy and number of the emitted photons are shown to be increased using the NCD plasma-filled cone target. Simulations are also performed to investigate the dependence of the electron energy, charge, and divergence angle on the plasma density for a given laser. Experimentally, the variation of the density can be achieved by adjusting the time delay between ns and ps laser pulses. These findings play important roles in the development of high-energy-density experiments, including radiography and ultrafast diagnostics. Additionally, one main challenge of using NCD plasma-filled cone target in experiments is the alignment between the laser spot and the entrance of the cone. One potential solution is to use a larger laser spot and place a uniform NCD plasma layer before the cone, where the laser can first undergo a self-focusing process in the plasma lens[53] before coupling to the cone entrance.

Acknowledgements

Project supported by the Fund of the National Key Laboratory of Plasma Physics (Grant No. 6142A04230204) and the National Natural Science Foundation of China (Grant No. 12075046).

References

[1] Stark D J, Toncian T and Arefiev A V 2016 *Phys. Rev. Lett.* **116** 185003
[2] Jansen O, Wang T, Stark D J, d'Humières E, Toncian T and Arefiev A V 2018 *Plasma Phys. Control. Fusion* **60** 054006
[3] Zhao Z T, Wang D, Chen J H, *et al*. 2012 *Nat. Photonics* **6** 360
[4] Amann J, Berg W, Blank V, *et al*. 2012 *Nat. Photonics* **6** 693
[5] Allaria E, Castronovo D, Cinquegrana P, *et al*. 2013 *Nat. Photonics* **7** 913
[6] Martinez B, Barbosa B and Vranic M 2023 *Phys. Rev. Accel. Beams* **26** 011301
[7] He Y T, Blackburn T G, Toncian T and Arefiev A V 2021 *Commun. Phys.* **4** 139
[8] Vranic M, Klimo O, Korn G and Weber S 2018 *Sci. Rep.* **8** 4702
[9] Yakimenko V, Alsberg L, Bong E, Bouchard G, Clarke C, Emma C, Green S, Hast C, Hogan M J, Seabury J, Lipkowitz N, O'Shea B, Storey D, White G and Yocky G 2019 *Phys. Rev. Accel. Beams* **22** 101301
[10] Tajima T and Dawson J M 1979 *Phys. Rev. Lett.* **43** 267
[11] Gonsalves A J, Nakamura K, Daniels J, *et al*. 2019 *Phys. Rev. Lett.* **122** 084801
[12] Lu G W, Li Y J, Hu X C, Chen S Y, Xu H, Zhu M Y, Yan W C and Chen L M 2024 *Chin. Phys. B* **33** 064101
[13] Pukhov A, Sheng Z M and Meyer-ter-Vehn J 1999 *Phys. Plasmas* **6** 2847
[14] Rosmej O N, Shen X F, Pukhov A, Antonelli L, Barbato F, Gyrdymov M, Günther M M, Zähter S, Popov V S, Borisenko N G and Andreev N E 2021 *Matter Radiat. Extremes* **6** 048401
[15] Babjak R, Willingale L, Arefiev A and Vranic M 2024 *Phys. Rev. Lett.* **132** 125001
[16] Geng P F, Lv W J, Li X L, Tang R A and Xue J K 2018 *Chin. Phys. B* **27** 035201
[17] Hussein A E, Arefiev A V, Batson T, Chen H, Craxton R S, Davies A S, Froula D H, Gong Z, Haberberger D, Ma Y, Nilson P M, Theobald W, Wang T, Weichman K, Williams G J and Willingale L 2021 *New J. Phys.* **23** 023031
[18] Shaw J L, Romo-Gonzalez M A, Lemos N, King P M, Bruhaug G, Miller K G, Dorrer C, Kruschwitz B, Waxer L, Williams G J, Ambat M V, McKie M M, Sinclair M D, Mori W B, Joshi C, Chen H, Palastro J P, Albert F and Froula D H 2021 *Sci. Rep.* **11** 7498
[19] Morimoto Y and Baum P 2018 *Nat. Phys.* **14** 252
[20] Huang T W, Robinson A P L, Zhou C T, Qiao B, Liu B, Ruan S C, He X T and Norreys P A 2016 *Phys. Rev. E* **93** 063203
[21] Tang H, Tangtartharakul K, Babjak R, Yeh I L, Albert F, Chen H, Campbell P T, Ma Y, Nilson P M, Russell B K, Shaw J L, Thomas A G R, Vranic M, Arefiev A V and Willingale L 2024 *New J. Phys.* **26** 053010
[22] Gahn C, Tsakiris G D, Pukhov A, Meyer-ter-Vehn J, Pretzler G, Thirolf P, Habs D and Witte K J 1999 *Phys. Rev. Lett.* **83** 4772
[23] Willingale L, Thomas A G R, Nilson P M, Chen H, Cobble J, Craxton R S, Maksimchuk A, Norreys P A, Sangster T C, Scott R H H, Stoeckl C, Zulick C and Krushelnick K 2013 *New J. Phys.* **15** 025023
[24] Huang T W, Zhou C T, Zhang H, Wu S Z, Qiao B, He X T and Ruan S C 2017 *Phys. Rev. E* **95** 043207
[25] Ceurvorst L, Ratan N, Levy M C, Kasim M F, Sadler J, Scott R H H, Trines R M G M, Huang T W, Skramic M, Vranic M, Silva L O and Norreys P A 2016 *New J. Phys.* **18** 053023
[26] Najmudin Z, Krushelnick K, Tatarakis M, Clark E L, Danson C N, Malka V, Neely D, Santala M I K and Dangor A E 2003 *Phys. Plasmas* **10** 438
[27] Xiao K D, Huang T W, Zhou C T, Qiao B, Wu S Z, Ruan S C and He X T 2016 *AIP Advances* **6** 015303
[28] Zhu X L, Liu W Y, Chen M, Weng S M, McKenna P, Sheng Z M and Zhang J 2022 *Phys. Rev. Appl.* **18** 044051
[29] Huang T W, Zhou C T, Robinson A P L, Qiao B, Zhang H, Wu S Z, Zhuo H B, Norreys P A and He X T 2015 *Phys. Rev. E* **92** 053106
[30] Ju L B, Huang T W, Xiao K D, Wu G Z, Yang S L, Li R, Yang Y C, Long T Y, Zhang H, Wu S Z, Qiao B, Ruan S C and Zhou C T 2016 *Phys. Rev. E* **94** 033202
[31] Zheng X L, Zhang X M and Shen B F 2024 *Phys. Plasmas* **31** 083104
[32] Gong Z, Mackenroth F, Wang T, Yan X Q, Toncian T and Arefiev A V 2020 *Phys. Rev. E* **102** 013206
[33] Ji L L, Jiang S, Pukhov A, Freeman R and Akli K 2017 *High Power Laser Sci. Eng.* **5** e14
[34] Jiang S, Ji L L, Audesirk H, George K M, Snyder J, Krygier A, Poole P, Willis C, Daskalova R, Chowdhury E, Lewis N S, Schumacher D W, Pukhov A, Freeman R R and Akli K U 2016 *Phys. Rev. Lett.* **116** 085002

[35] Pan Z, Liu J B, Wang P J, Mei Z S, Cao Z X, Kong D F, Xu S R, Liu Z P, Liang Y L, Peng Z Y, Xu T Q, Song T, Chen X, Wu Q F, Zhang Y J, Han Q H, Chen H R, Zhao J R, Gao Y, Chen S Y, Zhao Y Y, Yan X Q, Shou Y R and Ma W J 2024 *Phys. Plasmas* **31** 043108

[36] Shou Y R, Wang D H, Wang P J, *et al*. 2021 *Opt. Lett.* **46** 3969

[37] Zhang J, Wang W M, Yang X H, Wu D, M Y Y, Jiao J L, Zhang Z, Wu F Y, Yuan X H, Li Y T and Zhu J Q 2020 *Phil. Trans. R. Soc. A* **378** 20200015

[38] MacPhee A G, Divol L, Kemp A J, *et al*. 2010 *Phys. Rev. Lett.* **104** 055002

[39] Kamboj O, Ghotra H S, Thakur V, Pasley J and Kant N 2021 *Eur. Phys. J. Plus* **136** 484

[40] Nakamura T, Sakagami H, Johzaki T, Nagatomo H, Mima K and Koga J 2007 *Phys. Plasmas* **14** 103105

[41] Ebert T, Heber R, Abel T, Bieker J, Schaumann G and Roth M 2021 *High Power Laser Sci. Eng.* **9** e24

[42] Yu T P, Yu W, Shao F Q, Luan S X, Zou D B, Ge Z Y, Zhang G B, Wang J W, Wang W Q, Li X H, Liu J X, Ouyang J M and Wong A Y 2015 *J. Appl. Phys.* **117** 023105

[43] Xue K, Dou Z K, Wan F, Yu T P, Wang W M, Ren J R, Zhao Q, Zhao Y T, Xu Z F and Li J X 2020 *Matter Radiat. Extremes* 054402

[44] Li X M, Chao Y, Xie R, Liu D J, Zhou Y Z, Zhang S T, Yang T, Liu Z J, Cao L H and Zheng C Y 2022 *Laser Part. Beams* **e24** 2022

[45] Rosmej O N, Andreev N E, Zaehter S, Zahn N, Christ P, Borm B, Radon T, Sokolov A, Pugachev L P, Khaghani D, Horst F, Borisenko N G, Sklizkov G and Pimenov V G 2019 *New J. Phys.* **21** 043044

[46] Ma B B, Ren J R, Wang S Y, *et al*. 2022 *Laser Part. Beams* **2022** e15

[47] Rosmej O N, Gyrdymov M, Andreev N E, Tavana P, Popov V, Borisenko N, Gromov A I, Gus'kov S Y, Yakhin R, Vegunova G A, Bukharskii N, Korneev P, Cikhardt J, Zähter S, Busch S, Jacoby J, Pimenov V G, Spielmann C and Pukhov A 2025 *High Power Laser Sci. Eng.* **13** e3

[48] Yuan X X, Zhou C T, Zhang H, Li R, Ping Y L and Zhong J Y 2023 *Chin. Phys. B* **32** 054101

[49] Arber T D, Bennett K, Brady C S, Lawrence-Douglas A, Ramsay M G, Sircombe N J, Gillies P, Evans R G, Schmitz H, Bell A R and Ridgers C P 2015 *Plasma Phys. Control. Fusion* **57** 113001

[50] Pan K Q, Li Z C, Guo L, Gong T, Li S W, Yang D, Zheng C Y, Zhang B H and He X T 2023 *High Power Laser Sci. Eng.* **11** e76

[51] Shou Y R, Wang P J, Lee S G, *et al*. 2023 *Nat. Photonics* **17** 137

[52] Zhu X L, Yin Y, Yu T P, Shao F Q, Ge Z Y, Wang W Q and Liu J J 2015 *New J. Phys.* **17** 053039

[53] Shou Y R, Lu H Y, Hu R H, Lin C, Wang H Y, Zhou M L, He X T, Chen J E and Yan X Q 2016 *Opt. Lett.* **41** 139